Magnetic Machine Perception for Reconstruction of Nonuniform Electrical Conductivity Based on Eddy Current Model

Bingjie Hao, Kok-Meng Lee, *Fellow, IEEE*, and Ivy Chang

***Abstract*—This article presents a machine-perception method based on eddy current density (ECD) field induced in a plate for reconstructing nonuniform electrical conductivity. Formulated as a two-stage inverse problem using distributed current source models, the ECD field is reconstructed from its magnetic flux density and followed by solving an inverse ECD model to estimate the conductivity fields of the plate and its features. Along with a parametric study, the effects of different sensor and coil configurations on the reconstruction accuracy are numerically investigated. The proposed method is evaluated experimentally by comparing two methods: mechanical scanning using a single-sensor and a linear method with a sensitivity matrix. The findings demonstrate that using a sensor-array with a multicoil configuration effectively reduces the number of mechanical scans when making measurements, and eliminates variations below the coil center where the ECD is small.**

***Index Terms*—Conductivity, defect detection, eddy current (EC) imaging, inverse problem, reconstruction.**

I. Introduction

SENSING systems play an important role in both *in-situ* process monitoring and postfabrication quality inspection and failure analysis [1], [2], especially in additive manufacturing (AM) where various kinds of defects (such as poor surface finish, porosities, lack of fusion, inclusion, balling, cracks, and microstructure abnormity) of the AM parts must be inspected [3]. Many techniques (like optical, ultrasonic, electromagnetics, and x-ray) can be used to detect surface or subsurface properties. Among them, electrical conductivity is an important material parameter for metallic objects because it is directly related to residual stress [4], corrosion [5], and microstructure [6]; thus, it can be effectively used to inspect multimaterial composite AM parts with graded or separate regions of different materials [7].

Two most widely used methods [8] for conductivity detection are measurements based on four-point direct-current potential drop and eddy current (EC). Unlike the former which relies on the direct probe-to-object contact such that electrical current can be applied on the conductor, whereas the latter induces EC in the conductor, from which the conductivity is inferred from impedance change in the electromagnet (EM) coil or from measured magnetic flux density (MFD). EC-based methods are generally noncontact and have been widely used commercially in measurements of conductive plates with nonmetallic coating. Conventional EC sensing devices generally perform measurements with a single-point sensor, where the object being measured is assumed to have a uniform conductivity, ignoring edge effects. For applications where conductivity anomaly or defects exist in the conductor, single-point measurements that rely on mechanical scanning are inefficient. Instead, EC imaging or tomography techniques that visually present the conductivity distribution and features of defect through two-dimensional (2-D)/ three-dimensional (3-D) images have attracted more research interest. The methods can be used to locate defects, characterize local wall thinning in pipelines, and even detect abnormal tissues in medical applications [9].

A simple method for EC imaging is to use a single probe to perform a mechanical scan to form 2-D image [10], [11] which is, in reality, the assembly of point measurements that assume the neighboring conductivity or defect has no effect on the probe response. As an example, high-resolution conductivity images can be obtained by measuring the magnetic force due to EC through atomic force microscopy [11]. However, in many cases, the measured probe response at each point and the material and/or geometrical properties of the conductor are not in point–point correspondence. Additional inversion methods are required to translate the measured signal image to physical properties. For example, Pasadas *et al*. [12] reconstructed the perturbed EC distribution and visualized crack shape with 2-D eddy current density (ECD) images. Techniques like machine learning [10] and image processing are often used in the inversion process to reconstruct or characterize the shape and

Manuscript received January 7, 2020; revised March 13, 2020; accepted May 1, 2020. Date of publication May 6, 2020; date of current version October 14, 2020. This work was supported in part by the U.S. National Science Foundation under Grant CMMI-1662700, and in part by the National Basic Research Program of China (973 Program) under Grant 2013CB035803. Bingjie. Hao's research at Georgia Tech was financially sponsored by China Scholarship Council. Recommended by Technical Editor Y. Yuan and Senior Editor H. Ding. *(Corresponding author: Kok-Meng Lee.)*

Bingjie Hao is with the State Key Laboratory of Digital Manufacturing Equipment and Technology, Huazhong University of Science and Technology, Wuhan 430074, China. (e-mail: bjhao@hust.edu.cn).

Kok-Meng Lee and Ivy Chang are with the George W. Woodruff School of Mechanical Engineering, Georgia Institute of Technology, Atlanta, GA 30332 USA. (e-mail: kokmeng.lee@me.gatech.edu; ichang36@gatech.edu).

Color versions of one or more of the figures in this article are available online at https://ieeexplore.ieee.org.

Digital Object Identifier 10.1109/TMECH.2020.2992777

size of defects. Specially designed probes, such as biaxial EC probe and uniform magnetic field excitation are used to facilitate the deployment of inversion methods. Additionally, EC can be used with infrared thermal and magneto-optical imaging systems [13], [14] to achieve fast and large-scale EC imaging.

The above methods first construct measured electromagnetic images and then translate the image to a distribution of physical properties. In addition, the conductivity and defect distributions can be directly reconstructed from the measured EC responses. In these methods, EC models are often used to relate the conductivity or defect information with EC response. The main difficulty for the reconstruction method is the nonlinearity caused by mutual induction, which requires solving a complex inverse problem. Iterative method like Gauss–Newton method can be utilized to solve the problem for small number of conductivity variables, such as the reconstruction of 1-D conductivity profile [15]. For planar objects with much more conductivity unknowns, iterative-based method has the drawbacks of slow convergence speed and may fall into local minima. Therefore, noniterative reconstruction has attracted considerable interest [16], [17]. In [17], a linear superposition method was proposed to estimate the conductivity distribution from a set of measured MFDs, where a precalculated Jacobian matrix with each column representing the variation of measured MFD due to one and only one of the elements has abnormal conductivity. However, the assumption of linear superimposition only holds for defects with small deviation in conductivity.

As EC flowing through a nonmagnetic conductor depends on its conductivity, this article uses EC as a medium to reconstruct a conductivity distribution from its MFD. Modeled using a distributed current source (DCS) method originally proposed in [18] to derive closed-form solutions for describing the magnetic fields of an electromagnetic actuator and/or sensor, the ECD induced in a conductive plate was formulated as an optimization problem in [19] where the electric potential effects were neglected to solve the numerically discretized solutions. By explicitly accounting for the electric potentials in modeling the boundary constraints, closed-form solutions to the ECD problem were derived in [20]. In [20], where the conductor was discretized into volume elements (each with an ECD source) using the DCS method, the ECD problem was formulated as a forward EC model to solve for the ECD induced the conductive plate and its generated MFD for a given set of EM and conductor (geometrical and electrical) parameters. While still based on this forward EC model, this article presents a two-stage method that reconstructs the unknown conductivity distribution by conversely solving the inverse solutions to the EC model. Individual elemental conductivities are assigned to the DCS-based EC model to account for nonuniform conductivity distribution. The reconstruction method relaxes the linear assumption and does not require constructing a Jacobian matrix. The remainder of this article is organized as follows:

1) The forward EC model using DCS method [19], [20] is briefly introduced. Based on the forward model, the first stage reconstructs the ECD field from its EC-generated MFDs; and the second stage solves the inverse solution to the EC model.

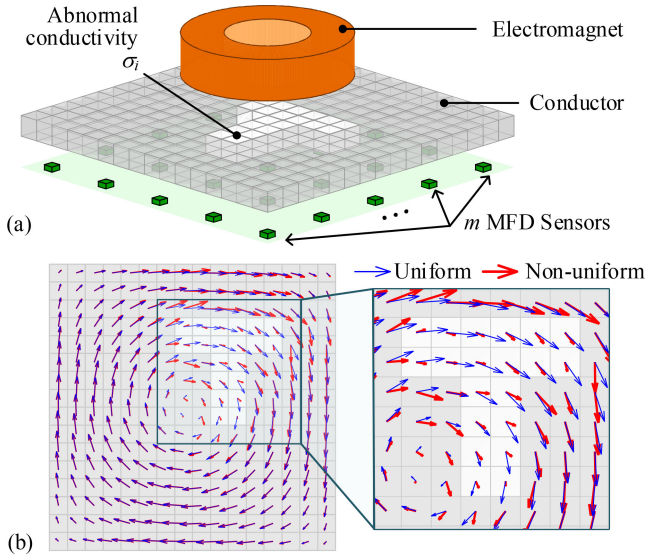

Fig. 1. Schematics illustrating EC-based conductivity reconstruction. (a) Sensing system. (b) ECD in conductor with a feature of abnormal conductivity.

2) The reconstruction method is numerically validated with MFD data simulated using finite element analysis (FEA). Parametric studies are conducted to analyze the effects of sensor configurations, multicoil excitation, and adaptive refinement on reconstruction accuracy and measurement efficiency of ECD and conductivity.
3) The effectiveness of the reconstruction method is evaluated experimentally with specimens containing a feature of different conductivity and local wall thinning. As will be shown, the reconstruction methods not only can detect abnormal conductivity but also can measure nonuniform thickness equivalent to conductivity anomaly.

II. Method

Fig. 1 shows a typical EC-based sensing system to detect abnormal conductivity in a nonferrous conductive plate that has a targeted feature (for example, the T-shaped region of abnormal conductivity) to be measured. As alternating current flows through the EM placed above the plate, it generates an alternating electric field $\mathbf{E}$ according to Faraday's law and induces an ECD $\mathbf{J}$ that obeys Ohm's law ($\mathbf{J} = \sigma\,\mathbf{E}$) in the conductor. Theoretically, the conductivity σ for a given current input to the EM can be inferred from $\mathbf{J}$, which can be determined from EC-generated MFD measurements using MFD sensors placed near the plate. However, $\mathbf{J}$ and σ have a complicated relationship since $\mathbf{E}$-field is unknown due to mutual induction among conductor elements. Therefore, a physical model that accounts for mutual induction is required to describe the relation between $\mathbf{J}$ and σ.

A. Formulation of EC-Based Measurement Models

The ECD distribution can be computed numerically, for example, using DCS models with $\mathbf{J}$-φ formulation [20]. The DCS modeling method decomposes the conductive plate into

n hexahedral elemental volumes, each of which (ith element) is characterized by an ECD source $\mathbf{j}_i = [J_{ix}, J_{iy}, J_{iz}]^{\mathrm{T}}$ and conductivity σ_i. The ith element source can be modeled as

$$\mathbf{j}_i = -\sigma_i \frac{\partial}{\partial t}\left(\mathbf{A}_{\mathbf{e}i} + \mathbf{A}_{\mathbf{v}i}\right) - \sigma_i \nabla \varphi_i \tag{1a}$$

where

$$\mathbf{A}_{\mathbf{e}i} = \mathbf{f}_{\mathbf{e}i} u \text{ and } \mathbf{A}_{\mathbf{v}i} = \sum_{l=1}^{n} f_{vil} \mathbf{j}_l \tag{1b, c}$$

In (1a), $\mathbf{A}_{\mathbf{e}i}$ and $\mathbf{A}_{\mathbf{v}i}$ are the magnetic vector potentials (MVPs) contributed by the excitation coil and volume elemental current sources in the conductor, respectively; u is the input current through the EM coil, and φ_i is the elemental electric potential. In (1b, c), $\mathbf{f}_{\mathbf{e}}$ and f_v are the respective kernel functions [18] describing the MVP generated by a unit-current EM and unit-current density sources.

With (1a–c), the EC system with sinusoidal excitation input can be compactly expressed in discrete representation. Noting that (u and $\mathbf{J}$) can be replaced with ($j\omega u$ and $j\omega\mathbf{J}$) using phasor method, the *system* equation is given by (2) as follows:

$$(\mathbf{I} + j\omega\sigma_0 \mathbf{S}\mathbf{F})\,\mathbf{J} + \sigma_0 \mathbf{S}\boldsymbol{\Gamma}\boldsymbol{\Phi} = -j\omega\sigma_0 \mathbf{S}\mathbf{b}u \tag{2}$$

where

$$\mathbf{J}(\in \mathbb{C}^{3n\times 1}) = [\mathbf{j}_1^{\mathrm{T}} \cdots \mathbf{j}_i^{\mathrm{T}} \cdots \mathbf{j}_n^{\mathrm{T}}]^{\mathrm{T}}$$
$$\boldsymbol{\Phi}(\in \mathbb{C}^{n\times 1}) = [\varphi_1 \cdots \varphi_i \cdots \varphi_n]^{\mathrm{T}}$$
$$\mathbf{S}(\in \mathbb{R}^{3n\times 3n}) = diag(\boldsymbol{\sigma} \otimes [1\ 1\ 1]^{\mathrm{T}})$$

$\boldsymbol{\sigma} = \frac{1}{\sigma_0}[\sigma_1 \cdots \sigma_i \cdots \sigma_n]^{\mathrm{T}}$; σ_0 is the reference conductivity, and $\mathbf{I}$ is a $3n$-by-$3n$ identity matrix.

In (2), $\mathbf{b}(\in \mathbb{R}^{3n\times 1})$ and $\mathbf{F} \in \mathbb{R}^{3n\times 3n}$ are associated with the kernel functions ($\mathbf{f}_{\mathbf{e}}$, f_v); and $\boldsymbol{\Gamma}(\in \mathbb{R}^{3n\times n})$ is the gradient operation matrix. The vector $\mathbf{b}$ and matrices, $\mathbf{F}$ and $\boldsymbol{\Gamma}$, can be precalculated if the detailed geometry of the conductor is known. To solve (2) for a physically relevant solution, the continuity equation $\nabla \cdot \mathbf{J} = 0$ [20] must be satisfied; this *constraint* equation can be represented by $(n-1)$ discrete equations given in (3) where $\mathbf{Q}(\in \mathbb{R}^{(n-1)\times 3n})$:

$$\mathbf{Q}\mathbf{J} = \mathbf{0}. \tag{3}$$

The system (2), along with the constraint (3) for ECD and $\mathbf{Q}_p\boldsymbol{\Phi} = 0$ (that designates the zero potential for $\boldsymbol{\Phi}$) forms a set of linear equations, the solutions ($\mathbf{J}$ and $\boldsymbol{\Phi}$) to which can be solved if the conductivity matrix $\mathbf{S}$ is specified.

The EC-generated MFD $\mathbf{B}$ can be measured by a set of m sensors [Fig. 1(a)], which can be mathematically expressed as an *output* (4), where $\mathbf{C}(\in \mathbb{R}^{3m\times 3n})$ and $\mathbf{B}(\in \mathbb{C}^{3m\times 1})$:

$$\mathbf{C}\mathbf{J} = \mathbf{B}. \tag{4}$$

Collectively, (2) and (3) are referred to here as the forward model of the EC system, and (4) is a measurement equation.

As an illustration, Fig. 1(b) compares the ECD fields in the conductive plate with/without a T-shaped region of abnormal conductivity, which are denoted by (red, blue) arrows; the latter (plate with uniform conductivity) provides a basis for comparison. The ECD deviation $\Delta\mathbf{J}(= \mathbf{J} - \bar{\mathbf{J}})$ and corresponding measurements $\Delta\mathbf{B}(= \mathbf{B} - \bar{\mathbf{B}})$ relative to that induced in a uniform conductor $\bar{\mathbf{J}}$ and its EC-generated MFD $\bar{\mathbf{B}}$ are utilized to reconstruct the conductivity field and detect hidden features in plate, where $\bar{\mathbf{J}}$ and $\bar{\mathbf{B}}$ are precalculated from the forward model (2–4) for plates with uniform conductivity. As the unknown conductivity cannot be directly determined from MFD, its reconstruction from measured $\Delta\mathbf{B}$ data is formulated as a two-stage *inverse* problem. The first *stage* solves for $\Delta\mathbf{J}$ to reconstruct the ECD distribution $\bar{\mathbf{J}} + \Delta\mathbf{J}$. Once $\mathbf{J}$ is reconstructed, the second *stage* recasts (2) into a regression problem to construct the conductivity distribution.

Stage I: Reconstruction of the ECD field

The ECD deviation $\Delta\mathbf{J}$, which occurs not only the nonuniform region but also the region surrounding it, must satisfy the continuity (3) and can be inferred from measured deviation $\Delta\mathbf{B}$ through the output (4). Thus, the relationship between the unknown $\Delta\mathbf{J}$ and the measured $\Delta\mathbf{B}$ is formulated in (5a) as follows:

$$\boldsymbol{\beta} = \boldsymbol{\alpha}\Delta\mathbf{J} + \boldsymbol{\eta} \tag{5a}$$

where $\boldsymbol{\alpha} = [\mathbf{C}^{\mathrm{T}}\ \mathbf{Q}^{\mathrm{T}}]^{\mathrm{T}}, \boldsymbol{\beta} = [\Delta\mathbf{B}^{\mathrm{T}}\ \mathbf{0}]$, and $\boldsymbol{\eta}$ is the measurement noise. The solution $\Delta\mathbf{J}$ can be solved with the regularization method to prevent overfitting due to measurement noise and insufficient measurement data [17]. Two most commonly used regularization techniques are L1 and L2 regularization. L1 regularization is prone to get sparse solutions (namely vector with more zero elements), which is not the case of $\Delta\mathbf{J}$ because the ECD deviation appear on all elements due to mutual induction. Instead, L2 regularization, also known as Tikhonov regularization, is commonly used for regularization of linear ill-posed problems. Compared with L1, solutions with L2 regularization can be computed more efficiently because the analytical solution is available. The solution $\Delta\mathbf{J}$ with L2 regularization can be directly solved in (5b) as follows:

$$\Delta\mathbf{J} = (\boldsymbol{\alpha}^{\mathrm{T}}\boldsymbol{\alpha} + \lambda\mathbf{I})^{-1}\boldsymbol{\alpha}^{\mathrm{T}}\boldsymbol{\beta}. \tag{5b}$$

$\Delta\mathbf{J}$ obtained from (5b) minimizes $\|\boldsymbol{\alpha}\Delta\mathbf{J} - \boldsymbol{\beta}\|^2 + \lambda\|\Delta\mathbf{J}\|^2$ where the regularization parameter λ can be determined using L-curve method [17]. The regularization term $\lambda\|\Delta\mathbf{J}\|^2$ implies that the deviation of ECD should be small such that the overall ECD distribution is similar to that of a uniform conductor.

Stage II: Reconstruction of the conductivity distribution

With estimated ECD, the real and imaginary parts of the 3-D vector $\mathbf{J} = \mathbf{J}_{\mathrm{Re}} + j\mathbf{J}_{\mathrm{Im}}$ in (2) can be written as

$$\mathbf{J}_{\mathrm{Re}} = \sigma_0 \mathbf{S}\left(\omega\mathbf{F}\mathbf{J}_{\mathrm{Im}} - \boldsymbol{\Gamma}\boldsymbol{\Phi}_{\mathrm{Re}}\right) \tag{6a}$$

$$\mathbf{J}_{\mathrm{Im}} = -\sigma_0 \mathbf{S}\left(\omega\mathbf{F}\mathbf{J}_{\mathrm{Re}} + \boldsymbol{\Gamma}\boldsymbol{\Phi}_{\mathrm{Im}} + \omega\mathbf{b}u\right). \tag{6b}$$

Assume that $\mathbf{S}$ is invertible. $\mathbf{S}$ and the unknown scalar vector $\boldsymbol{\Phi}$ $(= \boldsymbol{\Phi}_{\mathrm{Re}} + j\boldsymbol{\Phi}_{\mathrm{Im}})$ in (6a, b) are decoupled and rewritten as

$$\sigma_0\left(\omega\mathbf{F}\mathbf{J}_{\mathrm{Im}} - \boldsymbol{\Gamma}\boldsymbol{\Phi}_{\mathrm{Re}}\right) = \mathbf{S}^{-1}\mathbf{J}_{\mathrm{Re}} \tag{7a}$$

$$\sigma_0\left(\omega\mathbf{F}\mathbf{J}_{\mathrm{Re}} + \boldsymbol{\Gamma}\boldsymbol{\Phi}_{\mathrm{Im}} + \omega\mathbf{b}u\right) = -\mathbf{S}^{-1}\mathbf{J}_{\mathrm{Im}}. \tag{7b}$$

Denoting the three-directional components as $\ell(= x, y, z)$, (7a, b) can be decomposed into three component equation. Taking (7a) as an example, $\sigma_0(\omega\mathbf{F}_\ell\mathbf{J}_{\mathrm{Im}} - \boldsymbol{\Gamma}_\ell\boldsymbol{\Phi}_{\mathrm{Re}}) = \mathrm{diag}(\boldsymbol{\rho})\mathbf{J}_{\ell\mathrm{Re}}$,

where $\boldsymbol{\rho}$ is the bitwise inverse of $\boldsymbol{\sigma}$ denoting the normalized resistivity of the conductor elements. After extracting $\mathbf{F}_\ell$, $\boldsymbol{\Gamma}_\ell$, and $\mathbf{b}_\ell$ from the $3i-2$, $3i-1$, and $3i$ rows of $\mathbf{F}$, $\boldsymbol{\Gamma}$, and $\mathbf{b}$, we have

$$\hat{\mathbf{J}}_{\mathrm{Re}}\boldsymbol{\rho} + \sigma_0\hat{\boldsymbol{\Gamma}}\boldsymbol{\Phi}_{\mathrm{Re}} = \omega\sigma_0\hat{\mathbf{F}}\mathbf{J}_{\mathrm{Im}} \tag{8}$$

where

$$\hat{\mathbf{J}}_{\mathrm{Re}} = \begin{bmatrix} \mathrm{diag}(\mathbf{J}_{x\mathrm{Re}}) \\ \mathrm{diag}(\mathbf{J}_{y\mathrm{Re}}) \\ \mathrm{diag}(\mathbf{J}_{z\mathrm{Re}}) \end{bmatrix}; \hat{\mathbf{F}} = \begin{bmatrix} \mathbf{F}_x \\ \mathbf{F}_y \\ \mathbf{F}_z \end{bmatrix}; \hat{\boldsymbol{\Gamma}} = \begin{bmatrix} \boldsymbol{\Gamma}_x \\ \boldsymbol{\Gamma}_y \\ \boldsymbol{\Gamma}_z \end{bmatrix}$$

$$; \mathbf{b} = \begin{bmatrix} \mathbf{b}_x \\ \mathbf{b}_y \\ \mathbf{b}_z \end{bmatrix}.$$

The estimation of $\boldsymbol{\rho}$ from (8) is a regression problem. Utilizing Frisch–Waugh–Lovell theorem [21], $\boldsymbol{\Phi}_{\mathrm{Re}}$ can be dropped from (8) and the regression equation reduces to

$$\mathbf{M}\hat{\mathbf{J}}_{\mathrm{Re}}\boldsymbol{\rho} = \omega\sigma_0\mathbf{M}\hat{\mathbf{F}}\mathbf{J}_{\mathrm{Im}} \tag{9a}$$

where $\mathbf{M} = \mathbf{I} - \hat{\boldsymbol{\Gamma}}(\hat{\boldsymbol{\Gamma}}^{\mathrm{T}}\hat{\boldsymbol{\Gamma}})^{-1}\hat{\boldsymbol{\Gamma}}^{\mathrm{T}}$. Similarly, (7b) reduces to (9b) as follows:

$$\mathbf{M}\hat{\mathbf{J}}_{\mathrm{Im}}\boldsymbol{\rho} = -\omega\sigma_0\mathbf{M}(\hat{\mathbf{b}}u + \hat{\mathbf{F}}\mathbf{J}_{\mathrm{Re}}). \tag{9b}$$

Equation (9a) and (9b) can be combined into (10) as follows:

$$\begin{bmatrix} \mathbf{M}\hat{\mathbf{J}}_{\mathrm{Re}} \\ \mathbf{M}\hat{\mathbf{J}}_{\mathrm{Im}} \end{bmatrix}\boldsymbol{\rho} = \omega\sigma_0 \begin{bmatrix} \mathbf{M}\hat{\mathbf{F}}\mathbf{J}_{\mathrm{Im}} \\ -\mathbf{M}(\hat{\mathbf{b}}u + \hat{\mathbf{F}}\mathbf{J}_{\mathrm{Re}}) \end{bmatrix}. \tag{10}$$

For practical applications where the resistivity range of the abnormal region ($\boldsymbol{\rho} \in [\rho_{lb}, \rho_{ub}]$) is approximately known, the $\boldsymbol{\rho}$ estimation can be formulated as a constrained least-square (LS) problem that minimizes an error function $\|\mathbf{e}\|^2$:

$$\mathbf{e} = \begin{bmatrix} \mathbf{M}\hat{\mathbf{J}}_{\mathrm{Re}} \\ \mathbf{M}\hat{\mathbf{J}}_{\mathrm{Im}} \end{bmatrix}\boldsymbol{\rho} - \omega\sigma_0 \begin{bmatrix} \mathbf{M}\hat{\mathbf{F}}\mathbf{J}_{\mathrm{Im}} \\ -\mathbf{M}(\hat{\mathbf{b}}u + \hat{\mathbf{F}}\mathbf{J}_{\mathrm{Re}}) \end{bmatrix} \tag{11}$$

subject to $\rho_{\mathrm{lb}} \le \boldsymbol{\rho} \le \rho_{\mathrm{ub}}$. The conductivity vector $\boldsymbol{\sigma}$ can then be computed from the reciprocal of $\boldsymbol{\rho}$.

Because of the sequential computations, the estimation error of $\mathbf{J}$ in the first stage will affect the reconstructed conductivity. Therefore, sufficient measurement data are required for accurate reconstruction of the ECD and conductivity field from the solutions to the inverse model. A common method to increase data is to scan the conductor mechanically with a single-point MFD sensor, where a large dataset can be obtained but at the expense of measurement time. Alternatively, measurement data can be increased without sacrificing measurement efficiency by using multiple sequentially excited coils, through which additional sets of equations for solving the constrained LS problem (10) can be obtained. For a system sequentially excited with N coils, N sets of error functions $\mathbf{e}$ can be assembled as (12)

$$\min_{\boldsymbol{\rho}} \left\| \left[\mathbf{e}_1^{\mathrm{T}}, \mathbf{e}_2^{\mathrm{T}}, \ldots, \mathbf{e}_N^{\mathrm{T}}\right]^{\mathrm{T}} \right\|^2 \text{ subject to } \rho_{\mathrm{lb}} \le \boldsymbol{\rho} \le \rho_{\mathrm{ub}}. \tag{12}$$

B. Measurement Data for Conductivity Reconstruction

The following subsections discuss two criteria guiding the selection of measurements to improve the solutions to the inverse model. The first illustrates the reconstruction of a conductivity field using uniformly distributed measurement data. The second presents an adaptive method to increase measurements at the targeted region to enhance the boundary detection when detecting hidden conductive features.

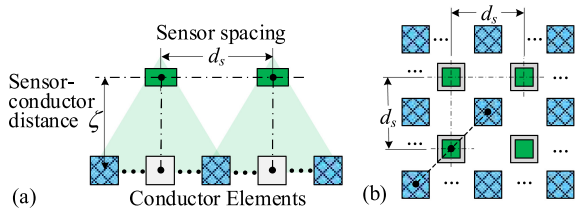

Fig. 2. Illustration of sensor parameters. (a) Front view. (b) Top view.

1) Measurement Data for Conductivity Reconstruction: The optimal solutions to (10) by minimizing (11) for a single coil or (12) for multiple coils provide a means to estimate the conductivity from the ECD $\mathbf{J}$ that can be reconstructed from measurements, each of which is the superposition of MFDs generated by nearby ECD elements as illustrated in Fig. 2 where MFD sensors are evenly spaced. For illustrative purposes, only the elements directly below the sensors (which are closest to a sensor) and elements in between four adjacent sensors (which are farthest from a sensor) are plotted. Other elements in between the closest and farthest elements, which are also measured by MFD sensors, are omitted in the figure. Since the MFD generated by an elemental ECD at the sensing point is inversely proportional to the square of the distance between them [18], the measurement data can be appropriately sized based on the ratio τ relating the MFD $|\mathbf{B}|_{\mathrm{L}}$ generated by the element farthest from a sensor (the blue elements with grid) to that $|\mathbf{B}|_{\mathrm{U}}$ closest to a sensor (the gray elements):

$$\tau = \frac{|\mathbf{B}|_{\mathrm{L}}}{|\mathbf{B}|_{\mathrm{U}}} = \frac{\left(\sqrt{2}\zeta\right)^2}{d_s^2 + \left(\sqrt{2}\zeta\right)^2} = \frac{1}{1 + 0.5(d_s/\zeta)^2}. \tag{13}$$

The ratio τ is selected between the [lower τ_l, upper τ_h] threshold values that satisfy $0 < \tau_l < \tau < \tau_h < 1$. The lower threshold τ_l ensures that the MFDs contributed by the ECD elements far from the sensor are included in the measurement, while τ_h keeps the sensors within their sensing range. For a sensor array with sensing points evenly spaced at interval d_s, the sensor–conductor distance ζ can be selected to meet the criterion specified in terms of the threshold values, τ_l and τ_h:

$$\sqrt{\frac{\tau_l}{2\left(1-\tau_l\right)}} < \frac{\zeta}{d_s} < \sqrt{\frac{\tau_h}{2\left(1-\tau_h\right)}}. \tag{14}$$

2) Adaptive Measurements for Conductive Feature Detection: To improve the detection accuracy of the hidden conductive features, a method based on the ECD deviation $\Delta\mathbf{J}$ to add measurement points adaptively near the boundary of the hidden feature is introduced. The vector field $\Delta\mathbf{J}$ is mainly distributed in the plane parallel to conductor surface; thus, the elemental ECD deviation can be characterized by tensor $\mathbf{G}$ and its norm T as given (15a, b), respectively:

$$\mathbf{G} = \begin{bmatrix} \partial\Delta J_x/\partial_x & \partial\Delta J_x/\partial_y \\ \partial\Delta J_y/\partial_x & \partial\Delta J_y/\partial_y \end{bmatrix} \tag{15a}$$

and

$$T = \sqrt{\text{trace}(\mathbf{G}^T\mathbf{G})}. \tag{15b}$$

New points are added in-between two adjacent measurements if T exceeds a predetermined threshold value. The method begins with an initial grid of measured MFD. The steps that adaptively add measurement points based on the ECD deviation $\Delta\mathbf{J}$ are briefly summarized as follows:

1) Calculate the tensor $\mathbf{G}$ at each element, and surf-fit them by a 2-D surface $T(x, y)$.
2) Halve the intervals between the MFD sensing points. For each newly added point, the normalized tensor norm $\kappa = (T - T_{\min})/(T_{\max} - T_{\min})$ is calculated. The new point is added to the measurements if κ is larger than a predetermined threshold T_{h1}:

$$\kappa = \begin{cases} > T_{h1} & \text{The new point is added to measurement.} \\ \leq T_{h1} & \text{Discard the point.} \end{cases}$$

3) To improve reconstruction accuracy, the measurement points can be further refined by repeating Step 2 until the spacing between any adjacent refined measurement points is comparable to the specified spacing between conductor elements. In the ith time refinement, new points are added to measurement if $\kappa > T_{hi}$ where $T_{h1} < T_{h2} < \cdots < T_{hi} < \cdots$.

III. Numerical Verification and Illustration

A numerical investigation has been conducted for verifying the EC model, and for design optimization of an EC-based sensing system; the latter uses the inverse solutions to analyze the effects of adaptive measurements and multiple coils on conductivity reconstruction.

A. Numerical Verification

The forward DCS-based EC model that accounts for nonuniform conductivity is validated by comparing its computed ECD (J_ℓ, where $\ell = x, y, z$) with $J_{\text{ref},\ell}$ simulated in COMSOL, a commercial FEA package. The results simulating the ECD induced by an EM in a square plate characterized by four conductivity quadrants ($\sigma_{\text{I}} = \sigma_{\text{III}} = \sigma_0$ and $\sigma_{\text{II}} = \sigma_{\text{IV}} = \sigma$) are presented in Fig. 3. Specifically, $\sigma/\sigma_0 = 1$: Plate (all four quadrants) has uniform conductivity $\sigma/\sigma_0 = 0$: second and fourth quadrants are electrically nonconductive.

As seen in Fig. 3(a) where the imaginary (Im) part of the ECD distribution for $\sigma = 0.2\sigma_0$ are compared, the ECD calculated by model and COMSOL are comparable. The ECD computing errors defined in (16) are shown in Fig. 3(b):

$$E_J = \frac{1}{J_{\max}} \times \sqrt{\frac{1}{n}\sum_{i=1}^{n}\sum_{\ell=x,y,z}\left(J_\ell^{\text{Re}} - J_{\text{ref},\ell}^{\text{Re}}\right)^2 + \left(J_\ell^{\text{Im}} - J_{\text{ref},\ell}^{\text{Im}}\right)^2}. \tag{16}$$

The errors are within 2% for the range of σ/σ_0 values, which increase somewhat with the conductivity difference.

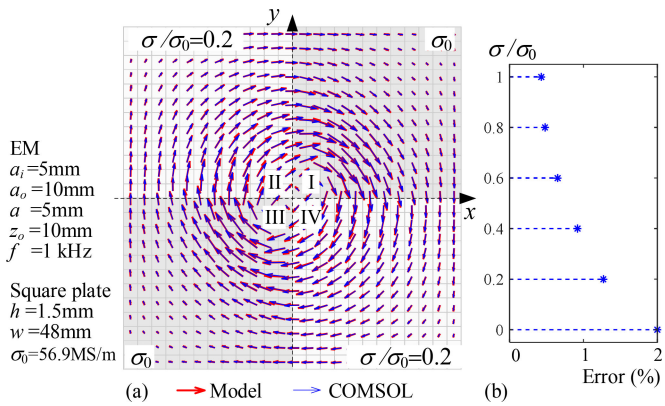

Fig. 3. Validation. (a) ECD distribution. (b) Computation errors.

TABLE I
SIMULATION PARAMETERS

(a) Sensor

(x, y) spacing = -20:ds:20
d_s = 10, 5, 2.5 mm
ζ = 2.5, 4.5, 6.5 mm

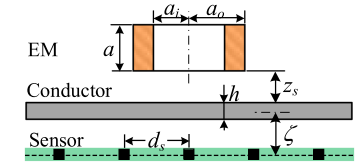

(b) EM coil

(a_o, a_i a) mm	(10, 5, 5)
z_s (mm)	9
Turns (#)	120
Wire dia. (mm)	0.36
f (Hz)	1000
R (Ω), L (μH)	0.95, 200

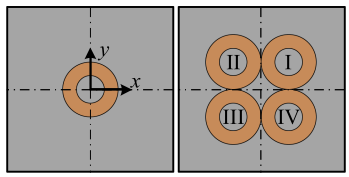

(c) Specimens

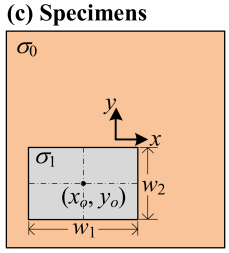

Square plate

$w \times w \times h$ (mm)	48×48×1.5
Element (mm)	2×2×1.5
σ_0 (MS/m)	56.9

Feature	(x_o, y_o) (mm)	$w_1 \times w_2$ (mm)	σ_1 (MS/m)
Square	(0, 0)	20×20	$0.1\sigma_0$
Rectangle	(4, 4)	24×16	$0.2\sigma_0$
Circle	(−4, −6)	12 (radius)	$0.3\sigma_0$

B. Data Size/Structure for Conductivity Reconstruction

The methods to improve the accuracy of conductivity reconstruction and feature detection without sacrificing measurement efficiency presented in Section II are best illustrated numerically. The system configurations, along with the location/size of the abnormal regions, used in the simulations are illustrated in Table I where the coordinate system is assigned at the plate center.

As shown in Table I, where the system configuration is defined (first row), an EC is induced in the (1.5-mm thick and 48-mm wide) square specimen by either one or four annular coils (second row) placed above it. The MFDs are measured by a 5 × 5 array of three-axis sensors in the plane on the other side of the plate, which is similar to an existing setup [17] designed to facilitate experimental validation in a laboratory setting. The

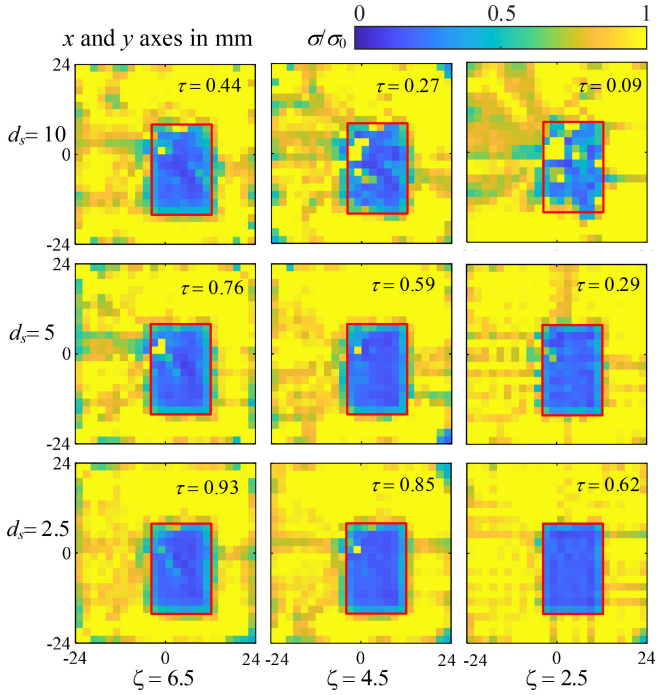

Fig. 4. Effects of sensor density and distance on reconstruction.

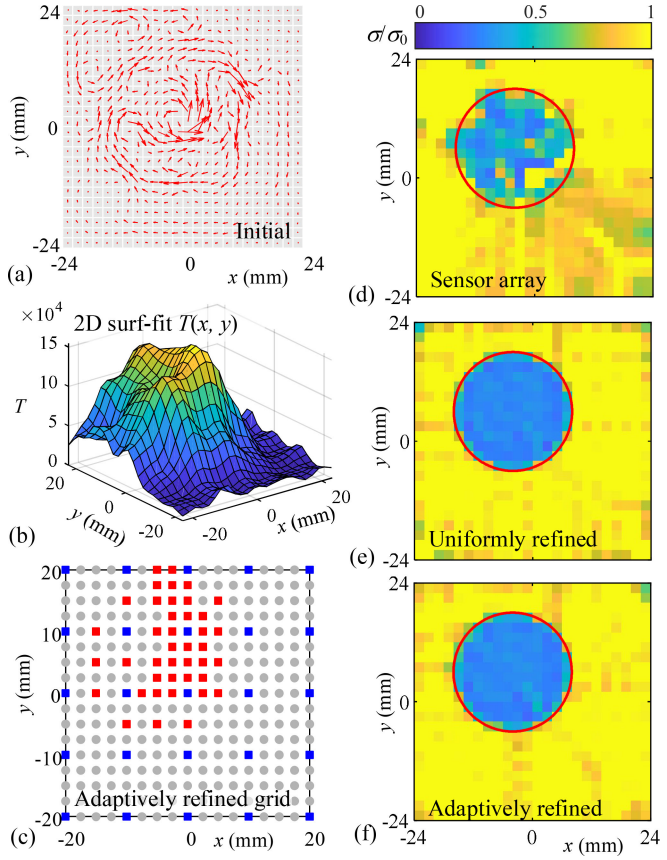

Fig. 5. Illustration of adaptive measurement points refinement method. (a) Initial reconstructed ECD deviation. (b) Norm of ECD tensor. (c) Illustration of measurement points. (d) Conductivity image from initial sensor array data (blue dots). (e) Results from uniformly refined data (blue + red + gray dots). (f) Results from adaptively refined data (blue + red dots).

coil(s) is/are applied with sinusoidal current(s) where the frequency f (=1 kHz) is selected to yield a skin-depth larger than plate thickness such that EC can penetrate the plate. The ECDs in the mid-plane of the square plate (across the thickness h) are computed in the following discussion. Three square plates (third row of Table I) with reference conductivity σ_0, each of which contains an abnormal region of different conductivity ($0.1\sigma_0$ square, $0.2\sigma_0$ rectangle, and $0.3\sigma_0$ circle) were simulated in COMSOL. The three different shapes, various positions of the shapes, and randomized conductivity values are chosen to demonstrate the robustness of the reconstruction method for a diversity of simulation samples. White noises (40-dB SNR) were added to the simulated MFD measurements for reconstructing the conductivity by solving (11) where the (lower and upper) bounds of the resistivity set at $(0.9\rho_0, 11\rho_0)$ where $\rho_0 = 1/\sigma_0$. MFDs in three-axis are measured in the range $[-20, 20]$ mm. The measured MFDs are contributed by both EM coils and ECDs in conductor, as the former is predetermined and thus can be subtracted to obtain the EC-generated MFD.

Three sets of simulations investigating the effects of *sensor parameters*, *data refinement*, and *multicoil configuration* on reconstruction are summarized in Figs. 4–7 and Table II. The estimations are evaluated in terms of the error defined in (17) where $(\sigma_i, \bar{\sigma}_i)$ are the (estimated, "true") conductivities of the ith conductor element and $\bar{\sigma}_i$ (used in COMSOL to simulate the forward model) serves as a basis for comparison:

$$E_\sigma = \frac{1}{n}\sum_{i=1}^{n}\frac{|\sigma_i - \bar{\sigma}_i|}{\sigma_0}. \tag{17}$$

1) Sensor parametric effects (Single coil)

TABLE II
CONDUCTIVITY ESTIMATION ERROR E_σ (MEAN, SD)

(a) Effect of data on estimation accuracy, Fig. 5(d~f), circle			
Method [# of measurements] (d_s, ζ) mm	**Sensor Array** [25] (10, 2.5)	**Additional scanned points**	
		Uniform [289] (2.5, 2.5)	**Adaptive** [65] (Non-uniform, 2.5)
E_σ	(0.14, 0.13)	(0.08, 0.08)	(0.08, 0.08)

(b) Effect of multi-coil on estimation accuracy, Fig. 6 (d_s= 5, ζ=4.5 mm)				
Features		**Square**	**Rectangle**	**Circle**
E_σ	1-coil [81]	(0.14, 0.11)	(0.12, 0.10)	(0.09, 0.08)
	4-coil [81×4]	(0.09, 0.09)	(0.07, 0.08)	(0.07, 0.07)

The *first* investigates the effects of sensor parameters (d_s, ζ) on conductivity reconstruction, from which the criteria for optimizing the sensor-conductor distance ζ bounded between the thresholds (τ_l, τ_h) are established. Typical results are depicted in Fig. 4 where the reconstructed conductivity images of the rectangle feature are shown to avoid repetitions. For each shape, the effects of nine d_s (= 10, 5, 2.5 mm) and ζ (= 2.5, 4.5,

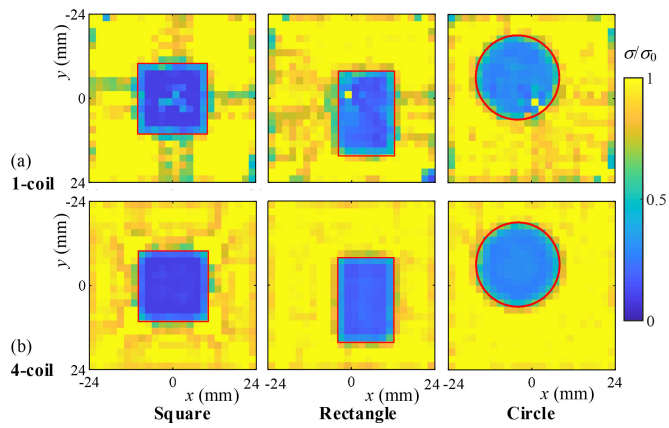

Fig. 6. Comparison of conductivity reconstruction results. (a) Single-coil configuration. (b) Four-coil configuration.

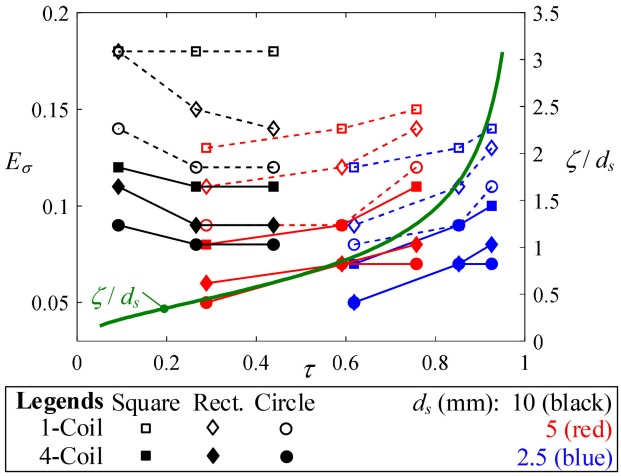

Fig. 7. Comparison of reconstruction errors.

6.5 mm) combinations on the conductivity estimation errors are compared in Figs. 4 and 7.

2) Adaptive refinement method (Single coil)

The *second* investigates the effects of adaptive refinement (commonly used to select points to improve measurement efficiency) on conductive feature detection. Fig. 5, where the circle feature is used as an example, illustrates the intermediate results of the adaptive refinement that begins with the initial 5×5 ($d_s = 10$ mm and $\zeta = 2.5$ mm) measurements:

Fig. 5(a): Reconstructed ECD field.
Fig. 5(b): 2-D surface surf-fit of the computed $T(x, y)$.
Fig. 5(c): Measurement points where blue dots indicate initial measurements ($d_s = 10$ mm); gray dots are 17×17 uniform points ($d_s = 2.5$ mm); and red dots are a subset of 17×17 points adaptively selected after two refinements ($T_{h1} = 0.5$ and $T_{h2} = 0.75$).

The right column compares the plate conductivity images reconstructed from three different datasets:

Fig. 5(d): 25 measurements with a 5×5 sensor array.
Fig. 5(e): 289 (17×17) uniformly spaced measurements
Fig. 5(f): 69 adaptively selected data.

Both the uniform and adaptive refinements are obtained by scanning the 5×5 sensor array mechanically (with 16 motion steps in each of the x and y directions). Unlike uniform refinement using all measurements in the formulation, the adaptive refinement discards points that did not satisfy the κ criteria. The mean and standard deviation (SD) of the conductivity estimation errors are compared in Table II.

3) Multicoil excitation

The *third* demonstrates the use of multicoils to improve reconstruction accuracy and efficiency. Unlike commonly used mechanical scanning methods that execute many measurements to extend sensing range, the multicoil configuration presents an efficient alternative that excites each coil to increase the number of measurements being taken without moving parts; and more importantly, the method is free from motion errors because the coils are stationary with respect to the sensor array. This article investigates the relationship between the number of additional measurements (free from motion-errors commonly associated with mechanical scanning) taken with the multicoil excitation configuration and conductivity estimation errors. Fig. 6 compares the conductivities of the three plates reconstructed using one and four coils (second row in Table I):

Single-coil: 81 (9×9) uniformly spaced data.
Four-coil: 324 ($9 \times 9 \times 4$) uniformly spaced data.

For both configurations, measurements are simulated with $d_s = \zeta = 4.5$ mm. It is worth noting that the four sets of 81 measurements in the four-coil configuration can be obtained simply by sequentially exciting the coils at different locations without additional motions. The conductivity estimation errors are compared in Fig. 7 and in Table II.

The findings in Figs. 4–7 and Table II are as follows:

1) Consider the first row of Fig. 4 where the effects of three sensor–conductor distances ($\zeta = 6.5$, 4.5, and 2.5 mm) for the given sensor spacing ($d_s = 10$ mm) on the reconstructed conductivity images are compared. The sparse measurements result in significantly high mean estimation errors E_σ in Fig. 7 (black dashed lines) particularly with a small ζ (=2.5) where the ECD elements close to the sensor dominate the measured MFD, while those between two sensors have little or no contributions. In contrast, with a large ζ (=6.5), more conductor elements including those far from the sensor contribute to the measured MFD; conceptually, ζ can be treated as a "filtering" parameter where the integral effect decreases the fluctuations due to noisy measurements but blurs the feature boundary. However, overly large ζ when measurements are dense have negative effects on reconstruction accuracy, as individual contributions of the elemental ECDs to each MFD sensor cannot be differentiated. The adverse effects of large ζ relative to small d_s can be observed in Fig. 4 ($d_s = 5$ mm in second row and $d_s = 2.5$ mm in third row), and in Fig. 7 where the mean errors are compared (red and blue dashed lines). Based on Fig. 7, the following guideline is used in

the subsequent studies:

$$\tau_l\,(=0.3) < \tau < \tau_h\,(=0.7)\,.$$

To facilitate sensor design, (13) that relates ζ/d_s to τ is plotted in Fig. 7 (green solid curve), where an appropriate ζ can be determined for a given d_s.

2) From the comparisons in Fig. 5(d)–(f) and in Table II(a), where the estimation errors are summarized, the two refinement (uniform and adaptive) methods yield nearly identical reconstructed conductivity and estimation errors, reducing the mean estimation error from 14% (initial 5×5 data) to 8%. However, compared with uniform method which requires additional 289 points for the measurement, the adaptive refinement method only requires 65 points (or less than 25% of the uniformly spaced data) to obtain similar accuracy; this finding suggests 1) significant time saving for applications where data are measured by mechanically scanning a single-point MFD sensor, and 2) mathematically reducing the dimension of the inverse problem for reconstruction.

3) Fig. 6(a) and (b) compares the conductivities reconstructed using one-coil and four-coil configurations. With a single coil [Fig. 6(a)], relatively large errors can be observed in the region under the coil center where the ECD is small. The four-coil configuration offers an effective means to resolve this problem; as shown in Fig. 6(b), the four-coil reconstruction shows fewer fluctuations in both feature and reference regions and a distinguishable boundary between them. As further demonstrated in Fig. 7 and Table II (b), the mean estimation errors of the four-coil reconstruction are between 7% and 9%, significantly lower than that reconstructed using the single-coil method (where $E_\sigma = 9\%$–14%) with the same sensor parameters ($d_s = 5$ mm, $\zeta = 4.5$ mm), particularly for features with sharp corners. Both the one-coil ($d_s = 2.5$ mm) and four-coil ($d_s = 5$ mm) reconstructions achieve similar accuracy; this finding demonstrates that the multicoil method does not rely on decreasing d_s (as in the single-coil method) to improve reconstruction accuracy.

IV. Experimental Results and Discussion

Two experimental investigations were conducted: The first validates the numerical simulations in Section III, which demonstrate the inverse EC model for conductivity reconstruction. The second evaluates the proposed method by comparing its estimation errors and measurement efficiency with that of a published method [17] based on linear Jacobian matrix. The two investigations were presented in Sections IV-A and IV-B and discussed in Section IV-C.

A. Experimental Validation

Experiments were conducted on the testbed [Fig. 8(a)], where the EC sensing system consists of an EM system [Fig. 8(b)] and existing MFD sensor array [17] [Fig. 8(c)]. To facilitate parametric studies in a laboratory setting, a fixture [Fig. 8(b)] is placed right below the EM system to hold

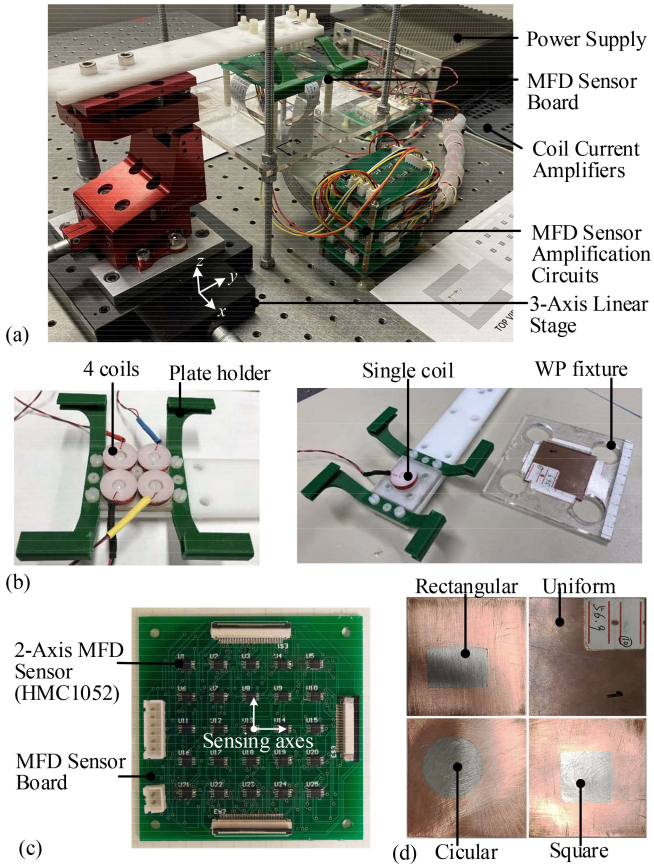

Fig. 8. Setup for first experimental investigation.

the specimen and positioned by a precision three-axis stage. Four 1.5-mm-thick square-plate specimens made from copper ($\sigma_0 = 56.9$ MS/m) were used, three of which were machined with a different shaped (square, rectangle, and circle) hole and filled with solder (Sn63/Pb37, $\sigma_1 = 6.9$ MS/m) to simulate nonuniform conductivity. The MFD sensor array contains 5×5 **two-axis** AMR sensors (HMC1052) which measure orthogonal MFDs in x and y directions (parallel to conductor surface). The sensors are equally spaced (10-mm interval) and placed at a distance $\zeta = 4.5$ mm on the opposite side of the EM. Compared with simulations, the sensors used in experiments lack the sensing axis in the z direction, which may affect the total number of MFD data available for reconstruction, but the proposed reconstruction method still applies because the lack of data can be compensated by adding more measurement points. By moving both the EM and plate together in the horizontal plane, much denser measurement points can be obtained for a given sensing array design. The EM is driven by a closed-loop current amplifier (KEPCO BOP 50-4M) which enables the current in EM proportional to excitation signal. The sinusoidal EM excitation signal ($f = 1000$ Hz) and measured MFD data are processed with NI DAQ devices (cDAQ-9178, NI 9205, and NI 9263). Other parameters including the dimension and location of the nonuniform regions can be found in Table I.

The voltage-to-MFD gain factor k of each sensing channel was calibrated using linear regression with simulated MFDs from the

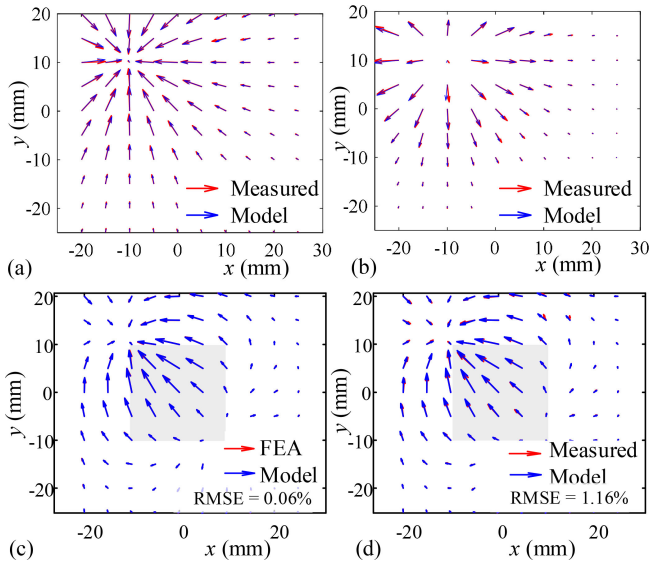

Fig. 9. Measured and simulated MFD. (a) Without plate. (b) Uniform plate. (c) Plate with square feature (model vs. FEA). (d) Plate with square feature (model vs. Experiment).

forward model [20]:

$$k = \sum_{i=1}^{m} V_i B_i / \sum_{i=1}^{m} V_i^2 \tag{18}$$

where m (=64) is the number of measurements obtained by placing the coils at different locations; V is the measured voltage; and B is the simulated MFD (without the conductive plate). Fig. 9(a) and (b), which correspond to measurements without and with a uniform plate in between the EM and sensors, compares the simulated and measured imaginary part of MFDs after calibration when the second coil is enabled; the normalized root-mean-square errors (RMSE) as defined in (19) are 0.64% and 0.51%, respectively.

$$B_{\mathrm{RMSE}} = \frac{1}{|\mathbf{B}_{\max}|} \times \sqrt{\frac{1}{n}\sum_{i=1}^{n}\sum_{\ell=x,y}\left(B_{\ell}^{\mathrm{Re}} - B_{\ell\mathrm{ref}}^{\mathrm{Re}}\right)^2 + \left(B_{\ell}^{\mathrm{Im}} - B_{\ell\mathrm{ref}}^{\mathrm{Im}}\right)^2}. \tag{19}$$

For numerical verification and experimental validation, the MFD generated by the induced ECD in the conductive plate with a square feature was simulated. The results simulated using the proposed DCS-based EC model are compared with that computed using COMSOL FEA and that experimentally obtained MFD data in Fig. 9(c) and (d) where only the real part of the MFD data are plotted to avoid repetitions. As compared in Fig. 9(c) and (d), the MFD data calculated by the DCS-based model agree excellently well with the FEA and experimental data (within a RMSE value of 0.06% and 1.16%, respectively), demonstrating the effectiveness of the EC model.

The experimental results are summarized in Figs. 10 and 11 and Table III. Fig. 10 shows the effect of multicoil excitation with $d_s = 2.5$ mm on the conductivity images of the copper plate with a square feature. The effects of sensor spacing ($d_s = 10$, 5, and 2.5) on the reconstructed conductivity using four-coil excitation are compared in Fig. 11, where red lines indicate the actual boundaries.

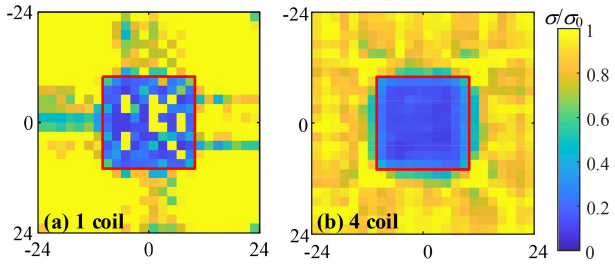

Fig. 10. Effect of multicoil excitations, $d_s = 2.5$ mm. (a) One-coil. (b) Four-coil.

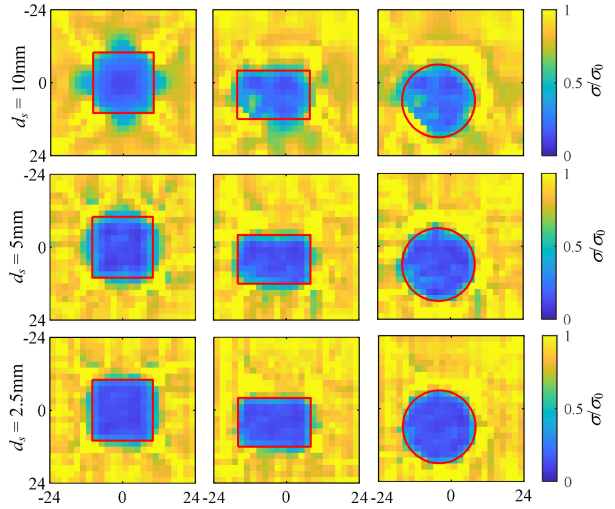

Fig. 11. Effects of different sensor intervals ($d_s = 10$, 5, 2.5) on reconstruction.

TABLE III
ESTIMATED σ/σ_0 (MEAN, SD) WITH FOUR-COIL EXCITATION

d_s(mm)	Region	Square	Rectangle	Circle
10	Feature σ_1	(0.29, 0.15)	(0.34, 0.19)	(0.36, 0.22)
	Plate σ_0	(0.85, 0.15)	(0.88, 0.14)	(0.89, 0.12)
5	Feature σ_1	(0.21, 0.11)	(0.22, 0.12)	(0.22, 0.11)
	Plate σ_0	(0.87, 0.13)	(0.91, 0.11)	(0.92, 0.10)
2.5	Feature σ_1	(0.18, 0.08)	(0.21, 0.10)	(0.20, 0.11)
	Plate σ_0	(0.89, 0.12)	(0.91, 0.10)	(0.92, 0.09)

The mean and SD of the conductivity reconstructed using four-coil excitation are shown in Table III, where the reconstructed conductivity σ is normalized to σ_0. Theoretically, the normalized plate and feature conductivities are 1 and σ_1/σ_0 (=0.12), respectively.

B. Local Wall Thinning Reconstruction

To provide a basis for benchmark comparisons and extend the reconstruction method to more general applications, an experimental investigation was conducted on a three-axis precision positioner (Fig. 12) to detect a local-wall-thinning (LWT) feature. Results are compared with recently published method based on

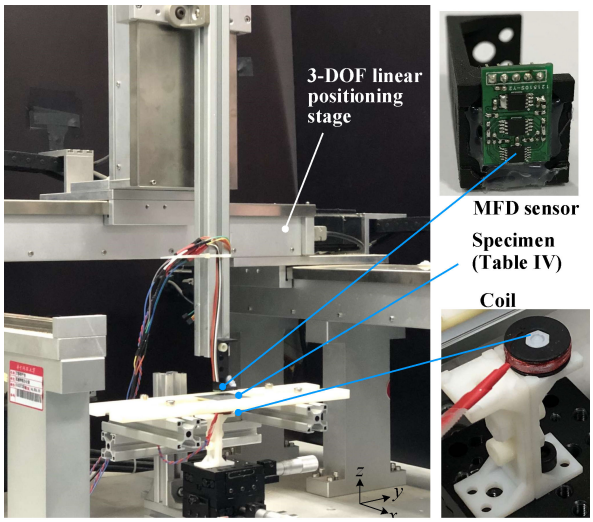

Fig. 12. Setup for second experimental investigation.

TABLE IV
EXPERIMENT PARAMETERS (ALUMINUM PLATE WITH T-POCKET)

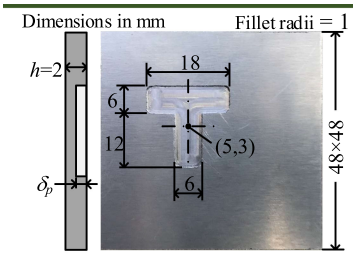

Square plate (48×48×2):	
σ_0 (MS/m)	24.7
δ_p	0.5, 1
DCS element size (number):	
2×2×2 (576)	
2-axis sensor (HMC1052):	
ζ	2, 4
d_s	2, 4
EM coil frequency	2 kHz

linear superposition [17] where an 882 × 576 Jacobian matrix was precalculated using the forward model for the reconstruction with 576 elemental conductors and 441 (two-axis) measurement points. The *i*th column of the precalculated matrix is the deviation of the EC-induced MFD in a uniform plate assuming that only *i*th element has an abnormal conductivity (equal to 90% of the normal value).

As shown in Fig. 12, the aluminum alloy plate was excited by a single EM coil that has the same characteristic values listed in Table I. The excitation coil and MFD sensor are placed on the opposite sides of the plate with the pocket facing the MFD sensor (programmed to scan in horizontal plane). The sensor is same with that used in Fig. 8 (two-axis AMR sensor that measures MFD in x and y directions). Two (2-mm thick and 48-mm wide) square plates made of aluminum alloy ($\sigma_0 = 24.7$ MS/m) were used, each of which has a T-shaped blind pocket of different depths (0.5 and 1 mm, corresponding to 25% and 50% of the plate thickness) at the bottom of the plate. The LWT region is blind T-pocket, which is modeled as an equivalent electrically nonuniform region with a conductivity lower than σ_0. As the method is based on the fact that EC in the LWT feature is smaller than that in the region of normal thickness, 2000-Hz excitation frequency was selected to ensure that the EC (with a skin-depth 2.26 mm) could penetrate the plate. Other parametric values are listed in Table IV.

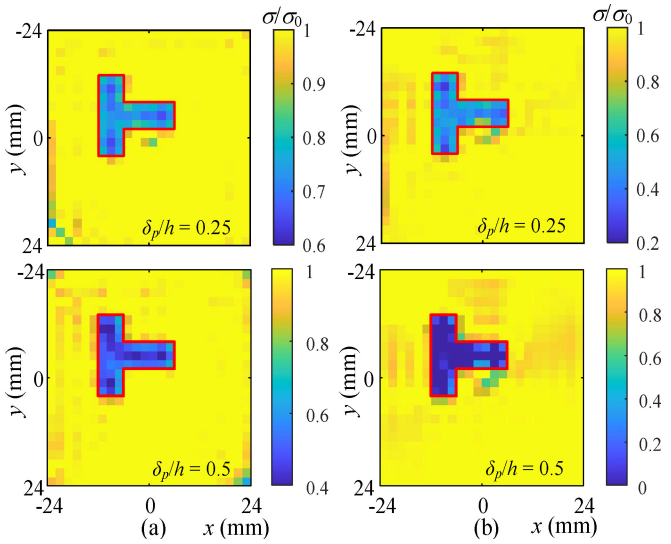

Fig. 13. Comparison between (a) proposed and (b) linearized methods.

TABLE V
T-POCKET REGION NORMALIZED CONDUCTIVITY (MEAN, SD)

δ_p/h	ζ	Proposed method $d_s=4$	Proposed method $d_s=2$	Linear method [17] $d_s=2$	Linear method [17] $d_s=4$
0.25	4	(0.75, 0.07)	(0.77, 0.06)	(0.52, 0.13)	(0.53, 0.14)
	2	(0.76, 0.08)	(0.74, 0.04)	(0.48, 0.10)	(0.53, 0.20)
0.5	4	(0.52, 0.08)	(0.55, 0.08)	(0.19, 0.24)	(0.17, 0.20)
	2	(0.53, 0.08)	(0.50, 0.07)	(0.17, 0.21)	(0.23, 0.28)
Time (s)					
Measurements		121	441	121	441
Comp.	**Offline**	7	13	492	502
	Online	0.5	0.55	0.2	0.24

The reconstruction results are summarized in Fig. 13 and Table V. Fig. 13 shows the estimated conductivity images for ($\zeta = 2$ mm, $d_s = 2$ mm). The (mean, SD) of the reconstructed elemental conductivities in the T-shape region, along with a comparison of measurement and computation times, are summarized in Table V for four (ζ, d_s) combinations.

C. Discussions of Results

Specific findings from the two experimental investigations in Sections III-A and B are as follows:

1) When the conductivity fields are reconstructed with conventional one-coil excitation, large variations can be seen in the region [Figs. 10(a) and 13] directly below the coil center where the ECD is small. As demonstrated in Figs. 10(b) and 11, these variations can be effectively eliminated using multicoil excitation at different locations.
2) As shown in Fig. 13, both the proposed method and the linear method (see Appendix) are capable of detecting the shape of the T-shaped blind pocket by treating the LWT as a region with a reduced conductivity. As shown in Table V, where the equivalent conductivities estimated by the two methods are compared, the conductivities

estimated using the linear method [17] are significantly smaller than the proposed method and exhibit large SD. In contrast, the conductivities estimated using the proposed method (that relaxes the superposition assumption by accounting for the nonlinear mutual induction effects in the EC model) are approximately 0.75 and 0.5 for the T-shaped pockets with δ_p/h = 0.25 and 0.5, respectively, which are essentially the normalized thickness $(1-\delta_p/h)$ of the LWT region. This finding suggests that the LWT thickness can be estimated, demonstrating an advantage over the linear method.

3) The tradeoff between accuracy and efficiency can be illustrated with Table V where the measurement and computation times are compared. Unlike the linearized model [17] that requires calculating the forward model 576 times when constructing the Jacobian matrix, the proposed model only needs to know the ECD and MFD of the conductor with uniform conductivity. The linearized model does not reconstruct ECD and thus requires less real-time computation (0.25 s) than the proposed model (0.5 s).
4) Table V illustrates the tradeoff between the sensor spacing ds (2 and 4 mm) and the sensor-to-plate distance ζ (2 and 4 mm); the latter has a filtering effect on the reconstruction. The reconstruction under ($d_s = \zeta = 2$, $\tau = 0.67$) yields the best thickness estimation with a smallest SD. When reconstructed with a small number of measurement points (or large $d_s = 4$), a better estimation is obtained with $\zeta = 4$ ($\tau = 0.67$) than $\zeta = 2$ ($\tau = 0.33$). On the other hand, the sensor should be close to the plate to minimize filtering effects for precise measurement with small interval.
5) Table III shows that the estimated plate conductivity is within 8% error when reconstructed with $d_s = 5$ and 2.5 mm. The feature conductivity is overestimated (larger than the actual value of 0.12) but the error (particularly its SD) decreases as ds reduces from 10 to 2.5 mm when reconstructed with the sensor-to-plate distance $\zeta = 4.5$ that has a filtering effect on the boundary. It is expected that the error can be further reduced (and hence a sharper boundary) with a smaller ζ as demonstrated in Table V.
6) Sensor array and multicoil configurations can effectively reduce the number of mechanical scans when making measurements. For example, 100 measurements can be made using a 5×5 sensor array with four-coil excitation, while a single-point sensor will require 100 mechanical scans.

V. Conclusion

A model-based method for reconstructing an EC induced in a nonmagnetic conductor and its electrical conductivity has been presented. Derived using DCS models in $\mathbf{J}-\varphi$ formulation, the EC model accounts for mutual induction between conductor elements; thus, the proposed method can handle a conductor with nonuniform conductivities.

The tradeoff between the sensor spacing d_s and the sensor-to-plate distance ζ which has a filtering effect on the feature boundary has been illustrated numerically. When reconstructed with a small number of measurement points, the estimation can be improved by increasing ζ. On the other hand, the sensor should be close to the plate to minimize filtering effects for precise measurement with small interval. Two techniques (adaptive measurement point refinement and multicoil excitation) were investigated to illustrate tradeoffs between accuracy and efficiency. Sensor array and multicoil configurations can effectively reduce the number of mechanical scans when making measurements.

Both the proposed method and the linear method are capable of detecting the shape of the T-shaped blind pocket by treating the LWT as a region with a reduced conductivity. However, the linear method [17] underestimates the equivalent conductivity and exhibits significantly large deviation in the estimated value. Experimental findings suggest that the LWT thickness can be estimated with the proposed method, demonstrating an advantage over the linear method.

Appendix

Linearized Model [17]

The linearized model supposes the reference conductivity σ_0 is known. The Jacobian matrix $\mathbf{G}(\in \mathbb{R}^{m\times n})$ that defined in (A.1) needs to be precalculated using forward model for n times, where m is the number of measurement data and n is the number of elements.

$$\mathbf{G} = [\partial \Delta \mathbf{B}/\partial \boldsymbol{\sigma}]^{\mathrm{T}}. \tag{A.1}$$

The ith column of $\mathbf{G}$ is given by (A.2) where B_{ij} is represents the jth MFD measurement by the conductor with conductivity σ_0 except the ith element has conductivity $(\sigma_0+\Delta\sigma)$, and $\bar{\mathbf{B}}$ is the MFD measurement by conductor with uniform conductivity.

$$\frac{\partial \Delta \mathbf{B}}{\partial \sigma_i} = \frac{1}{\Delta\sigma}\left([B_{i1}\cdots B_{ij}\cdots B_{im}]^{\mathrm{T}} - \bar{\mathbf{B}}\right). \tag{A.2}$$

The conductivity deviation of all elements is estimated from the deviation of actual measured EC-generated MFD $\mathbf{B}_{\mathrm{m}}$ relative to the MFD of the uniform conductor $\bar{\mathbf{B}}$ by solving (A.3):

$$\Delta\boldsymbol{\sigma} = \left(\mathbf{G}^{\mathrm{T}}\mathbf{G} + \lambda\mathbf{I}\right)^{-1}\mathbf{G}^{\mathrm{T}}\left(\mathbf{B}_{\mathrm{m}} - \bar{\mathbf{B}}\right) \tag{A.3}$$

where regularization method same with (5b) is used. Then, the estimated conductivity for the measured conductor is obtained as $\boldsymbol{\sigma} = \boldsymbol{\sigma}_0 + \Delta\boldsymbol{\sigma}$.

References

[1] H. Hoshyarmanesh, A. Abbasi, P. Moein, M. Ghodsi, and K. Zareinia, "Design and implementation of an accurate, portable, and time-efficient impedance-based transceiver for structural health monitoring," *IEEE/ASME Trans. Mechatron.*, vol. 22, no. 6, pp. 2809–2814, Dec. 2017.
[2] D. Mery, "Inspection of complex objects using multiple-x-ray views," *IEEE/ASME Trans. Mechatron.*, vol. 20, no. 1, pp. 338–347, Feb. 2015.
[3] S. K. Everton, M. Hirsch, P. I. Stavroulakis, R. K. Leach, and A. T. Clare, "Review of in-situ process monitoring and in-situ metrology for metal additive manufacturing," *Mater. Des.*, vol. 95, pp. 431–445, 2016.
[4] Y. Shen, C. C. H. Lo, A. M. Frishman, C. Lee, and N. Nakagawa, "Conductivity profile determination by eddy current for shot peened superalloy surfaces toward residual stress assessment," *AIP Conf. Proc.*, vol. 894, no. 1, pp. 1229–1236, 2007.

[5] Y. He, G. Tian, H. Zhang, M. Alamin, A. Simm, and P. Jackson, "Steel corrosion characterization using pulsed eddy current systems," *IEEE Sens. J.*, vol. 12, no. 6, pp. 2113–2120, Jun. 2012.
[6] X. Ma, A. J. Peyton, and Y. Y. Zhao, "Eddy current measurements of electrical conductivity and magnetic permeability of porous metals," *NDT E Int.*, vol. 39, no. 7, pp. 562–568, 2006.
[7] A. Bandyopadhyay and B. Heer, "Additive manufacturing of multi-material structures," *Mater. Sci. Eng. R: Rep.*, vol. 129, pp. 1–16, 2018.
[8] X. Chen and Y. Lei, "Electrical conductivity measurement of ferromagnetic metallic materials using pulsed eddy current method," *NDT E Int.*, vol. 75, pp. 33–38, 2015.
[9] R. Merwa, K. Hollaus, B. Brandstätter, and H. Scharfetter, "Numerical solution of the general 3D eddy current problem for magnetic induction tomography (spectroscopy)," *Physiol. Meas.*, vol. 24, no. 2, pp. 545–554, 2003.
[10] A. Bernieri, L. Ferrigno, M. Laracca, and M. Molinara, "Crack shape reconstruction in Eddy current testing using machine learning systems for regression," *IEEE Trans. Instrum. Meas.*, vol. 57, no. 9, pp. 1958–1968, Sep. 2008.
[11] V. Nalladega, S. Sathish, K. V. Jata, and M. P. Blodgett, "Development of eddy current microscopy for high resolution electrical conductivity imaging using atomic force microscopy," *Rev. Sci. Instrum.*, vol. 79, no. 7, 2008, Art. no. 073705.
[12] D. J. Pasadas, A. L. Ribeiro, T. Rocha, and H. G. Ramos, "2D surface defect images applying Tikhonov regularized inversion and ECT," *NDT E Int.*, vol. 80, pp. 48–57, Jun. 2016.
[13] A. Taram *et al.*, "Nondestructive testing of resistance spot welds using eddy current thermography," *Appl. Opt.*, vol. 57, no. 18, 2018, Art. no. D63.
[14] Y. Le Diraison, P. Y. Joubert, and D. Placko, "Characterization of subsurface defects in aeronautical riveted lap-joints using multi-frequency eddy current imaging," *NDT E Int.*, vol. 42, no. 2, pp. 133–140, 2009.
[15] W. Yin, S. J. Dickinson, and A. J. Peyton, "Imaging the continuous conductivity profile within layered metal structures using inductance spectroscopy," *IEEE Sens. J.*, vol. 5, no. 2, pp. 161–166, Apr. 2005.
[16] D. Placko, T. Bore, A. Rivollet, and P. Y. Joubert, "Original non-stationary eddy current imaging process for the evaluation of defects in metallic structures," *EPJ Appl. Phys.*, vol. 72, no. 1, 2015, Art. no. 10701.
[17] M. Li and K.-M. Lee, "Machine perception based on eddy current for physical field reconstruction of conductivity and hidden geometrical features," *IEEE Trans. Ind. Inform.*, vol. 15, no. 10, pp. 5392–5403, Oct. 2019.
[18] J. Lim and K.-M. Lee, "Distributed multilevel current models for design analysis of electromagnetic actuators," *IEEE/ASME Trans. Mechatron.*, vol. 20, no. 5, pp. 2413–2424, Oct. 2015.
[19] C.-Y. Lin, K.-M. Lee, and B. Hao, "Distributed current source method for modeling magnetic and eddy-current fields induced in nonferrous metallic objects," *IEEE/ASME Trans. Mechatron.*, vol. 23, no. 3, pp. 1038–1049, Jun. 2018.
[20] B. Hao, K.-M. Lee, and K. Bai, "Distributed current source modeling method for 3D eddy current problem in magnetic conductor with discrete state-space J-φ formulation," *J. Comp. Phys.*, vol. 401, 2020, Art. no. 109027.
[21] R. Frisch and F. V. Waugh, "Partial time regressions as compared with individual trends," *Econometrica: J. Econ. Soc.*, vol. 1, no. 4, pp. 387–401, 1933.

Bingjie Hao received the B.S. degree in mechanical engineering from the Huazhong University of Science and Technology (HUST), Wuhan, China, in 2014. He is currently working toward the Ph.D. degree in mechanical engineering with the School of Mechanical Science and Engineering, HUST.

He is a Visiting Scholar with the Woodruff School of Mechanical Engineering, Georgia Institute of Technology, Atlanta, GA, USA from October 2017 to October 2019. His research interests include sensing and control and mechatronics.

Kok-Meng Lee (Fellow, IEEE) received the B.S. degree in mechanical engineering from the State University of New York, Buffalo, NY, USA, in 1980, and the S.M. and Ph.D. degrees in mechanical engineering from the Massachusetts Institute of Technology, Cambridge, MA, USA, in 1982 and 1985, respectively.

He is currently a Professor with the George W. Woodruff School of Mechanical Engineering, Georgia Institute of Technology, Atlanta, GA, USA. His research interests include system dynamics/control, robotics, automation, and mechatronics.

Dr. Lee is a Life Fellow of the American Society of Mechanical Engineers. He was the recipient of the National Science Foundation Presidential Young Investigator, Sigma Xi Junior Faculty Research, International Hall of Fame New Technology, Kayamori Best Paper, IEEE/ASME Transactions on Mechatronics Best Paper, and Michael J. Rabins Leadership Awards.

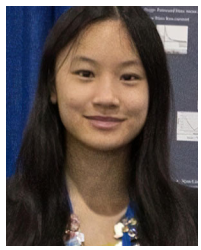

Ivy Chang received the B.S. degree in mechanical engineering from the Massachusetts Institute of Technology, Cambridge, MA, USA, in 2018. She is currently working toward the Ph.D. degree in mechanical engineering at Advanced Intelligent Mechatronics Research Laboratory, Georgia Institute of Technology, Atlanta, GA, USA.

Her research interests include robotic grasping, controls, and machine design.